PHYSICS

Bioinspired large Stokes shift small molecular dyes for biomedical fluorescence imaging

Hao Chen[1,2]†, Lingjun Liu[1,3]†, Kun Qian[1], Hailong Liu[1], Zhiming Wang[1], Feng Gao[1], Chunrong Qu[1], Wenhao Dai[1], Daizong Lin[1], Kaixian Chen[1,2,3], Hong Liu[1,2,3,4]*, Zhen Cheng[1,2,4]*

Long Stokes shift dyes that minimize cross-talk between the excitation source and fluorescent emission to improve the signal-to-background ratio are highly desired for fluorescence imaging. However, simple small molecular dyes with large Stokes shift (more than 120 nanometers) and near-infrared (NIR) emissions have been rarely reported so far. Here, inspired by the chromophore chemical structure of fluorescent proteins, we designed and synthesized a series of styrene oxazolone dyes (SODs) with simple synthetic methods, which show NIR emissions (>650 nanometers) with long Stokes shift (ranged from 136 to 198 nanometers) and small molecular weight (<450 daltons). The most promising SOD9 shows rapid renal excretion and blood-brain barrier passing properties. After functioning with the mitochondrial-targeted triphenylphosphonium (TPP) group, the resulting SOD9-TPP can be engineered for head-neck tumor imaging, fluorescence image–guided surgery, brain neuroimaging, and on-site pathologic analysis. In summary, our findings add an essential small molecular dye category to the classical dyes.

INTRODUCTION

Fluorescence imaging is widely used in preclinical biomedical research (1), clinical-pathological examination (2), and fluorescence image–guided surgery. It has the properties of low cost, easy to perform, minor light damage to the biological specimen, and high detection sensitivity (3). The biomedical applications of fluorescence imaging are highly dependent on the development of fluorescent dyes (4–6). The most critical features for fluorescent dyes are absorption/emission profile, absorption coefficient, quantum yield, Stokes shift, chemical property, and photochemical stability. However, few dyes have optimal properties in all of these categories. Several types of dyes, such as rhodamine, boron dipyrromethene (BODIPY), fluorescein isothiocyanate (FITC), cyanine, coumarin, and quinoline (7–16), have been widely used in clinical and preclinical research (Fig. 1A). These dyes show good application prospects in the clinic, biomedical research, and in vitro diagnosis. However, the emission wavelength of most of these dyes is less than 550 nm, which suffers from shallow penetration depth and notorious autofluorescence from biological tissues for in vivo optical imaging, broadly limiting their application. To obtain a sufficiently deep and sensitive signal for in vivo imaging, near-infrared (NIR) fluorescent dyes, including Nile red, cyanine dyes (Cy5, Cy5.5, and Cy7), IRDye800CW, indocyanine green (ICG), etc. have emerged as attractive tools. In contrast, most of them show short Stokes shift (<70 nm) (Fig. 1A). The heavy cross-talk between excitation and emission light leads to a relatively low signal-to-background ratio (SBR) (17).

Developing long Stokes shift NIR dyes is thus highly demanded, which loses less fluorescent light and results in high SBR in fluorescence imaging because of the complete separation of the excitation and emission light. Moreover, the dyes also allow multiplexing applications due to the flexibility of choosing excitation light and emission filters. The typical short Stokes' fluorophores use a relatively fixed single light source and emission filter (18). For decades, a great amount of effort has been dedicated to developing long Stokes shift NIR dyes, including the design of complicated structures and preparation of dyes through multistep reactions. Those efforts usually result in low synthesis yield and large conjugated rigid plane structure with high molecular weight, resulting in undesired pharmacokinetics, increased metabolism burden, and prolonged body accumulation time (19–26). Among most attempts, simple small molecular dyes with large Stokes shift (>120 nm) and NIR emissions have rarely been reported. The lack of chemical structure fluorescence relationship theory may contribute a lot to this scenario.

Biodistribution and pharmacokinetics are other essential features of small molecular dyes. Dyes with favorable in vivo behaviors have broad preclinical or clinical applications. In one respect, most central nervous system diseases are attributed to neurons' denaturation (27), while the specific mechanisms of pathogenesis are still unclear. To verify the pathogenesis, it is vital to find out the nerve cell's physiological activity and pathological process. Ginsberg et al. (28) used a sensitive, quantitative fluorescent method to study the time course and regional pattern of blood-brain barrier (BBB) opening after transient middle cerebral artery occlusion, demonstrating that neuronal activity can be observed with the aid of fluorescent dyes. Two/three-photon fluorescent microscopy has been widely used for brain science or neuron science imaging. However, one of the most substantial barriers in brain neuron science development is the BBB that hinders most of the dyes going into the brain. Few dyes could cross the BBB due to the large molecular weight and poor lipophilicity (29). The lack of BBB passing fluorescent dyes as imaging tools has hindered the development of brain science. Therefore, a small, compact NIR fluorophore (emission wavelength, >650 nm) that could rapidly penetrate the intact BBB is highly desired.

Furthermore, in the clinic, diagnosis of cancer/normal tissue in tumor surgery is crucial to improve recovery rates of tumor surgery

[1]State Key Laboratory of Drug Research, Molecular Imaging Center, Shanghai Institute of Materia Medica, Chinese Academy of Sciences, Shanghai 201203, China. [2]University of Chinese Academy of Sciences, No. 19A Yuquan Road, Beijing 100049, China. [3]State Key Laboratory of Natural Medicines and Department of Medicinal Chemistry, China Pharmaceutical University, 24 Tong Jia Xiang, Nanjing 210009, China. [4]Shandong Laboratory of Yantai Drug Discovery, Bohai Rim Advanced Research Institute for Drug Discovery, Yantai, Shandong 264117, China.
*Corresponding author. Email: zcheng@simm.ac.cn (Z.C); hliu@simm.ac.cn (H.L.)
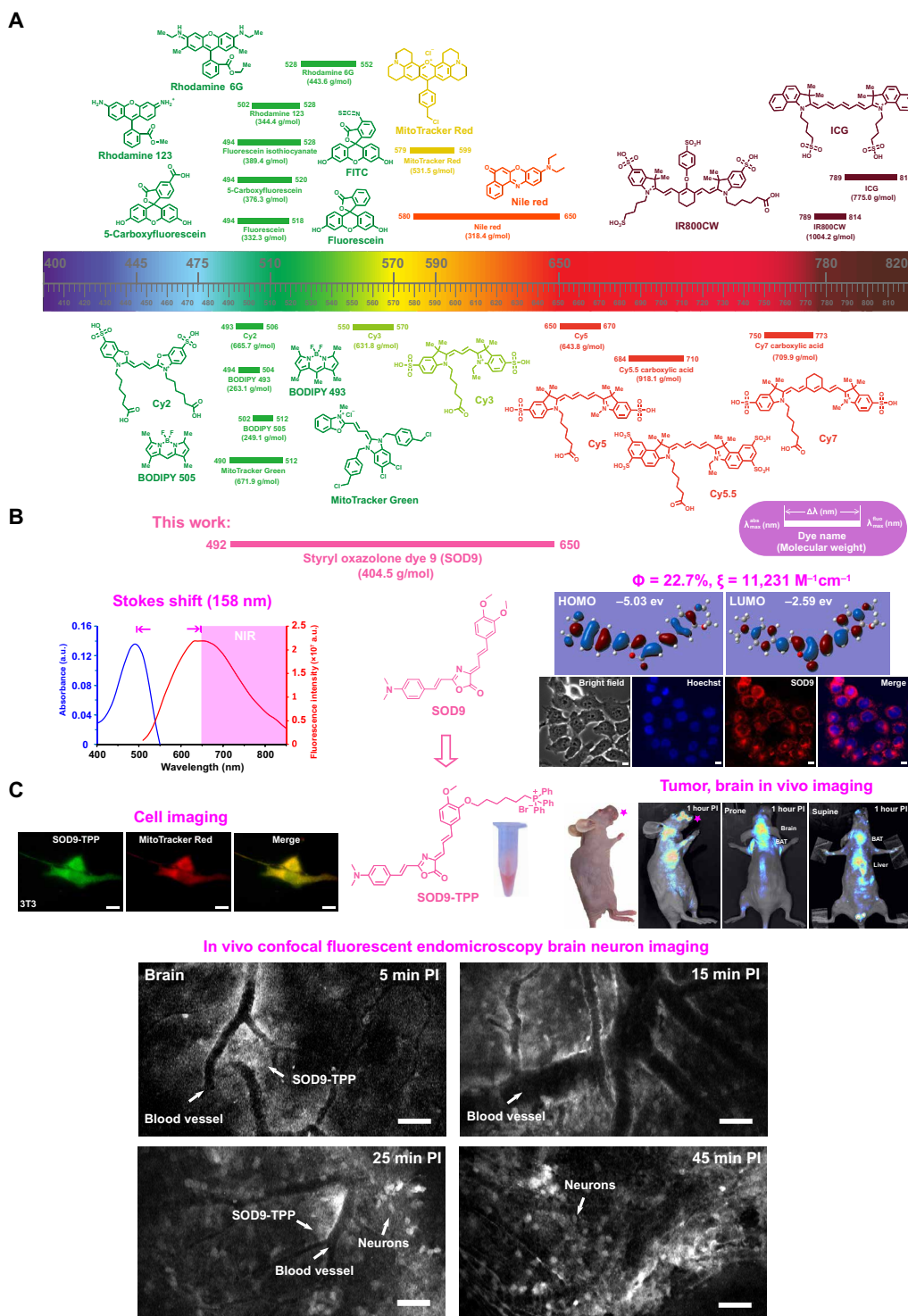†These authors contributed equally to this work.

Fig. 1. Long Stokes shift SOD for biomedical fluorescence imaging. (**A**) Chemical structure, molecular weight, max absorption, and emission wavelength, Stokes shift of typical commercial fluorescent dyes. (**B**) The absorption, fluorescence spectrum (left), chemical structure (middle), quantum yield, molar extinction coefficient (in water), computed isodensity surfaces of highest occupied molecular orbital (HOMO) and lowest unoccupied molecular orbital (LUMO), and cell imaging of the represent styrene oxazolone dye 9 (SOD9). (**C**) Triphenylphosphonium (TPP)–modified SOD9 for cell mitochondrial, in vivo head-neck cancer, and brain neuron imaging. a.u., arbitrary units; PI, post injection.

therapy and survival rates (*30*). Usually, clinical diagnosis depends on the hematoxylin and eosin (H&E) stain, which is time-consuming and inconvenient. Contrasted to the traditional clinical diagnosis and confocal microendoscopy, using fluorescence imaging to create a local image of human tissue with special fluorescent dyes is a faster and more promising approach. Although a wide variety of molecular dyes have been reported (*31–33*), only a few fluorescent dyes provide real-time monitoring of the physiological process and morbid state, since the tissue autofluorescence and probe cytotoxicity limit most of the dyes' applications (*34, 35*). Overall, there is a tremendous demand for fluorescent dyes with long Stokes shift, high biocompatibility and effectiveness, and BBB crossing properties.

Since being discovered in the 1960s (*36*), fluorescent proteins (FPs) have emerged as one of the most commonly used fluorophores. From green FP (GFP) to red FP (RFP), the relationship between the optical properties and the core chromophore chemical structure has been fully explored (*37, 38*). Learning from the FP chromophore evolution process would be an excellent method for developing long Stokes shift dyes (*39*). Here, inspired by the 4-(*p*-hydroxybenzylidene)-5-imidazolinone (*p*-HBI) chromophore conjugation changing that caused the redshift from the GFP to RFP, we designed and synthesized a series of styrene oxazolone dyes (SODs) as previously unreported dyes (Fig. 1B). These SODs showed superior optical and photochemical properties such as long Stokes shift (>130 nm), small molecular weight (<450 Da), easy modification, fast response, and low cytotoxicity (Fig. 1B). The most promising dye, SOD9, was then chosen for further in vitro and in vivo studies. Impressively, it showed a good capacity of the cell staining, rapid renal excretion, and BBB crossing properties (Fig. 1B). SOD9 conjugated with triphenylphosphonium moiety (SOD9-TPP) displayed selectively for brain neurofluorescence imaging with not obviously toxic. Moreover, SOD9-TPP accumulated in the orthotopic head and neck squamous cell carcinoma (HNSCC) for in vivo fluorescence imaging, which simplified tumor diagnosis, fluorescence image–guided tumor surgery, and on-site pathologic analysis (Fig. 1C). This study reports the first high-efficiency SODs as long Stokes shift dyes, which add an essential small molecular dye category to the classical dyes and provide a new strategy for in vivo fluorescence imaging.

RESULTS

Design and synthesis of SODs

FPs have been widely studied and used in biological research. It is conceived that the FPs generally share the same core skeleton of imidazolinone moiety and an exocyclic double bond, depending on the *cis-trans* isomerism of the fluorescent chromophore to switch between the dark state and the bright state (*40*). Despite the rigidity of the FP chromophore, the main peculiarity of the core skeleton is the isomerization and protonation progress of the chromophore responsible for protein fluorescent occurring with light or pH changes, causing neutral *trans* isomer (off-state) to anionic *cis* isomer (on-state) (*41*). While imaging the dynamic process of the occurrence and development of biological processes, it is considered that fluorescence keeps on-state all the time. Given that the off-state of FP chromophore with twisted intramolecular charge transfer arises from the exocyclic double-bond configuration, structural modifications can be performed to inhibit the rotation.

In another aspect, FP chromophore essentially serves as one of the small molecular dyes for biomedical fluorescence imaging. One of the most common methods to increase the fluorescence imaging sensitivity and quantification capability is using long Stokes shift NIR small molecular dyes (*42, 43*). Donor (D)–π-acceptor (A)–π-donor (D) architecture is a common platform for constructing an organic fluorescent probe with a long Stokes shift to lower the energy gap and extend the wavelength (*33, 44*). Usually, the rate constant of intersystem transition from π* to π is small, enhancing fluorescent efficiency and favoring fluorescent occurrence (*45*).

Inspired by *p*-HBI chromophore of the GFP/RFP and the molecular mechanisms described above (Fig. 2A), we designed and synthesized a series of previously unreported dyes with styrene oxazolone as a fundamental skeleton instead of the imidazolinone (Fig. 2B and fig. S1). Unexpectedly, we found that this modification inhibits the rotation of the exocyclic double bond, leading the configuration to keep as *cis*-isomer (on-state), which was confirmed by x-ray (fig. S2). It saves room for structural modification, resulting in improved optical properties with extending Stokes shift. A conjugated structure with a rigid plane can lower molecular vibration frequency to strengthen fluorescence intensity by decreasing interaction with dissolvent (*46*). *N*,*N*′-dimethylamino is a well-known redshift absorption-pushing group when substituted on the para-position of an aromatic ring (*47*). The existence of oxazolone offered both π-π–conjugated and p-π–conjugated effects. Thus, we selected *N*,*N*′-dimethylamino
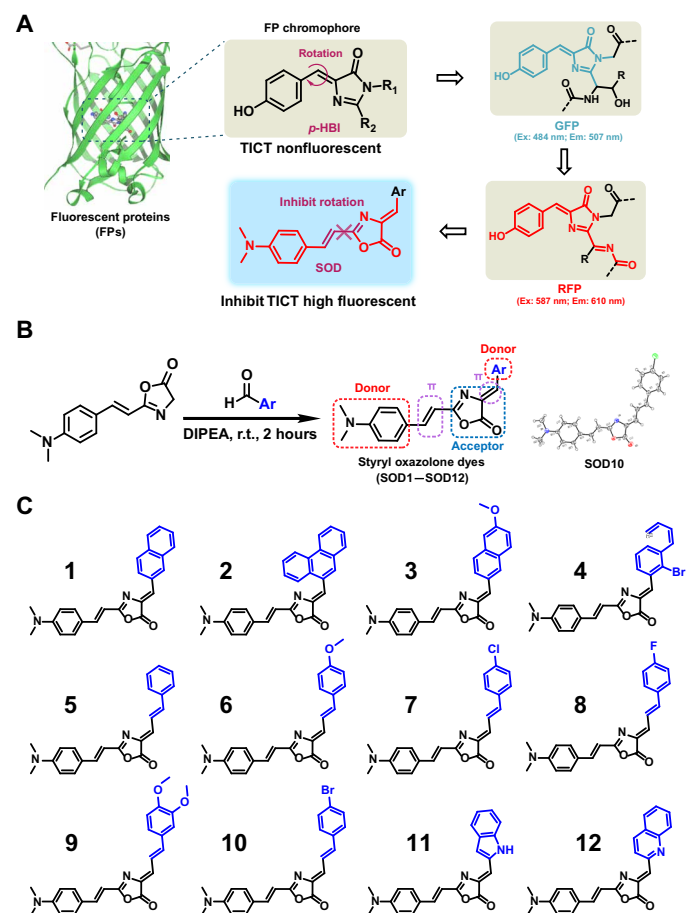
Fig. 2. Design and synthesis of SODs. (**A**) The chromophore chemical structures of GFP and RFP. (**B**) Synthesis of SODs (left) and the crystal structure of SOD10 (right). DIPEA, *N*,*N*-Diisopropylethylamine. (**C**) The chemical structures of SOD dyes. Ex., excitation; Em., emission; TICT, twisted intramolecular charge transfer; r.t., room temperature.

group and oxazolone as the donor and acceptor groups, respectively, linked by phenylethylene. We introduced another donor moiety on the central component to generate a neutral form, making the system more polarized and shifting to a red region. Following the described strategy, SODs were synthesized with a simple procedure. Oxazolone derivatives, generated from cinnamylic acid via condensation, reacted with different aldehydes under room temperature within 2 hours to afford SODs in good yields. The chemical structures of SODs (Fig. 2C) were characterized by standard ^{1}H nuclear magnetic resonance (NMR), ^{13}C NMR, and high-resolution mass spectrometry spectra in the Supplementary Materials.

Characteristics of SODs

We first investigated their spectroscopic properties in aqueous media. Because of the presence of *cis*-configuration of the exocyclic

double bond, all the SOD dyes displayed strong fluorescence. Most of them exhibited long Stokes shift (136 to 198 nm), with their absorption wavelengths at around 485 nm and fluorescence emission wavelengths over 635 nm (Fig. 3, A, B, and E). All of the SOD dyes showed good photostability, except SOD8, which bleached markedly over a 45-min test (Fig. 3C). Different substituted groups at the donor side had a negligible effect on the dyes' absorption spectrum but substantial affected the fluorescence spectrum (Fig. 3, D and E). The extension of the π system led to a redshift fluorescence spectrum (SOD1 versus SOD2). SOD4 showed the most notable fluorescence and Stokes shift, indicating that fluorescence redshift benefited from the electron-withdrawing group substituted by naphthalene (SOD1 and SOD3 versus SOD4). Meanwhile, the electron-donating group resulted in a fluorescence spectrum blueshift (SOD5 versus SOD6). Fluoro-substituted SOD8 demonstrated the shortest
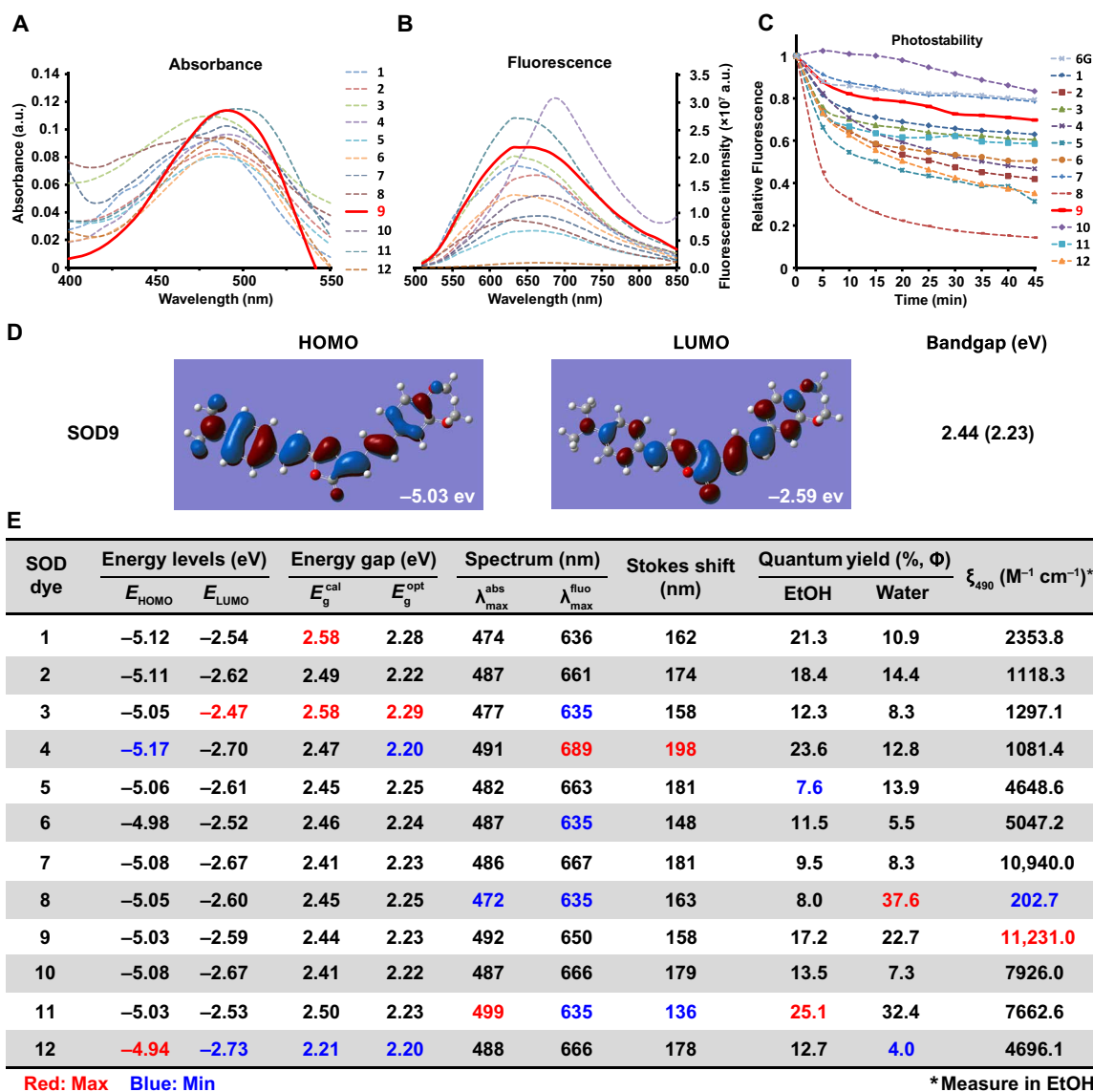

Fig. 3. Optical characteristics of SODs. The absorbance (**A**), fluorescence spectrum (**B**), and photostabilities (**C**) of SODs were measured in water with the concentration of 20, 12, and 10 μM, respectively (6G represents rhodamine 6G). (**D**) Density functional theory (DFT) optimized molecular orbital plots (HOMO and LUMO) of SOD9. (**E**) The optical properties summary of SOD dyes. Red is the maximum value, and blue is the minimum value of the same column. EtOH, ethanol.

SOD dye	Energy levels (eV)		Energy gap (eV)		Spectrum (nm)		Stokes shift (nm)	Quantum yield (%, Φ)		ξ_{490} (M^{-1} cm^{-1})*
	E_{HOMO}	E_{LUMO}	E_g^{cal}	E_g^{opt}	λ_{max}^{abs}	λ_{max}^{fluo}		EtOH	Water	
1	−5.12	−2.54	2.58	2.28	474	636	162	21.3	10.9	2353.8
2	−5.11	−2.62	2.49	2.22	487	661	174	18.4	14.4	1118.3
3	−5.05	−2.47	2.58	2.29	477	635	158	12.3	8.3	1297.1
4	−5.17	−2.70	2.47	2.20	491	689	198	23.6	12.8	1081.4
5	−5.06	−2.61	2.45	2.25	482	663	181	7.6	13.9	4648.6
6	−4.98	−2.52	2.46	2.24	487	635	148	11.5	5.5	5047.2
7	−5.08	−2.67	2.41	2.23	486	667	181	9.5	8.3	10,940.0
8	−5.05	−2.60	2.45	2.25	472	635	163	8.0	37.6	202.7
9	−5.03	−2.59	2.44	2.23	492	650	158	17.2	22.7	11,231.0
10	−5.08	−2.67	2.41	2.22	487	666	179	13.5	7.3	7926.0
11	−5.03	−2.53	2.50	2.23	499	635	136	25.1	32.4	7662.6
12	−4.94	−2.73	2.21	2.20	488	666	178	12.7	4.0	4696.1

Red: Max   Blue: Min   ***Measure in EtOH**

absorption/fluorescence and the highest relative quantum yield in water, implying fluorine's substantial and unique effect on the optical property. Other researchers also found a similar phenomenon (48). Another interesting finding was SOD11, which contained the indole as the donor group. It showed the largest absorption and the lowest fluorescence peak, resulting in the shortest Stokes shift.

The difference in spectroscopic properties could be derived from the electrical property and the position of substituents. Screening the bandgap by density functional theory (DFT) calculation and the actual measurement, all SODs had a similar bandgap identified with the absorption and fluorescence wavelengths (Fig. 3, D and E, and figs. S3 and S4). SOD4 exhibited the largest Stokes shift (198 nm). Notably, SOD8 and SOD11 displayed sufficiently high relative fluorescence quantum yield in water or alcohol (ϕ = 37.6 and 25.1, rhodamine 6G as the reference).

The molar absorption coefficients (ε) of SODs were around 1.0×10^3 to 1.0×10^4 M^{-1} cm^{-1}, except for SOD8, which was about 200 M^{-1} cm^{-1} (Fig. 3E). The highest ε was SOD9, similar to GFP or RFP as 1.0×10^4 M^{-1} cm^{-1}, which perhaps contributed to the structural similarity. Compared to the high ε cyanine dyes such as Cy5 (2.5×10^5 M^{-1} cm^{-1}) and ICG (2.621×10^5 M^{-1} cm^{-1}), SOD dyes were not so dominant. But considering the widely used GFP and RFP, the ε of some SODs, such as SOD7 and SOD9, was enough for fluorescence imaging applications.

In summary, a variety of factors affect the optical properties of SODs. The poor electron condensed ring attaching to the exocyclic double bond showed a redshift spectrum than the electron-rich one. The same result was found on the substituted polycyclic aromatic attaching to the exocyclic double bond as diolefins. Furthermore, for the same substitution group, multiple substituents showed better spectral properties than single substituents. In addition, the characteristics of SOD dyes were affected by various elements such as rigidity, solubility, and steric hindrance. Compared to rhodamine, some SODs showed good photostability (Fig. 3C).

Cytotoxicity of SODs was also examined on NIH-3T3 cell lines by 3-(4,5-dimethylthiazol-2-yl)-2,5-diphenyl tetrazolium bromide (MTT) assay. The results indicated that these dyes were nontoxic, demonstrating the good biological characteristics of those dyes (fig. S5). The cell uptake properties of SODs were investigated on the NIH-3T3 cell line (Fig. 4A and fig. S6) by fluorescent microscopic imaging. Fluorescence images showed that most SODs easily crossed the cell membrane, except SOD2, SOD4, SOD8, SOD10, and SOD12 (fig. S6). No specific organelle accumulation was found in SODs by fluorescent microscopy organelle costain experiment. Considering the optical spectrum, Stokes shift, quantum yield, and molar absorption coefficient, SOD9 stood out with the most attractive properties and was selected for further study.

SOD9's in vivo pharmacokinetics by fluorescence imaging
Before in vivo fluorescence imaging, the in vivo imaging setup's excitation wavelength and emission collection filter were screened out by directly imaging the SOD9 phosphate-buffered saline (PBS) solution in 1.5-ml Eppendorf tubes (fig. S7A). The excitation wavelength was set at 535 nm, and the collection wavelength was set at 659 nm (bandwidth, ~10 nm) because of the relatively longer wavelength and higher fluorescent intensity (fig. S7B). After this, in vivo fluorescence imaging was performed. A substantial fluorescent signal was observed in mice's bladder after the intravenous injection of SOD9 into mice (n = 3 per group) at 2.5 mg/kg (6.18 µmol/kg)

within 5 min (Fig. 4B). The bladder signal disappeared in 1.5 hours (Fig. 4C), indicating that SOD9 featured a fast renal excretion pathway (Fig. 4D). Notably, the fluorescence in the brain was also found by 5 min postinjection (Fig. 4B). This implied that the dye quickly passed the BBB. After 2 hours postinjection, the mice were euthanized, and the major organs were harvested for ex vivo fluorescence imaging. The biodistribution result showed that SOD9 mainly presented in the mice's brain and gallbladder. In addition, SOD9 also minorly existed in the bladder. Signal was also observed from brown adipose tissue (BAT), white adipose tissue (WAT), intestine, and stomach (49, 50). The high fluorescence in the gallbladder proved that SOD9 was also excreted by the liver. The fast high accumulation and relatively long retention time of SOD9 in mice brains suggested that the dye crossed the BBB. It can be used for central nervous system fluorescence imaging, which most commercially available dyes do not accomplish. It is presumably owing to the low molecular weight and charge-free nature of SOD9.

In vivo pharmacokinetics and biomedical applications of SOD9-TPP
To demonstrate the use of SOD9 for biomolecule labeling, the alkylation reagent SOD9-Br was synthesized by simply changing the appropriate starting materials of SOD9 (fig. S8). Although SOD9-Br can be used to label a variety of biomolecules, such as DNA, RNA, protein, and antibody, here, we used it to label a mitochondria-targeted small molecule, triphenylphosphonium (TPP) salt, for general fluorescence imaging applications (Fig. 5A). TPP and its analogs are classical delocalized lipophilic cations (DLCs), famous for mitochondrial-targeted applications. They work as cargos to deliver dyes to most cells' mitochondria due to the positive charge of the compounds and the mitochondrial membrane potential (51, 52). Through conjugation, TPP with SOD9 renders the resulting probe capability of staining cells, tissues, and organs. In addition, DLCs can also specifically accumulate in cancer cells due to the natural mitochondrial membrane potential difference between cancer cells ($\Delta\Psi c$, approximately −220 mV) and normal cells ($\Delta\Psi n$, approximately −140 mV), which could be used for the specific in vivo imaging of tumor (53, 54). The molecular weight of SOD9-TPP was almost doubled as that of the original SOD9 (815 Da versus 404 Da; Fig. 5A). With all of the above expectations, SOD9-TPP was synthesized in a high yield. Incubation of SOD9-TPP with NIH-3T3 and U87MG human glioblastoma cells and then costaining with MitoTracker Red and LysoTracker Red proved that SOD9-TPP's mitochondria specifically targeted property in vitro (Fig. 5B, fig. S9, and movie S1). The mean fluorescent intensities of SOD9-TPP in NIH-3T3, U87MG, and SCC090 cell lines were compared with the same incubation concentration and time. The result showed that the probe accumulated much more in the tumor cells than in normal cells, which proved its tumor-specific targeting properties (fig. S10).

After in vitro imaging of SOD9-TPP in normal and cancer cells, the in vivo biocompatibility was evaluated by intravenous injection of SOD9-TPP (5.0 mg/kg) into mice. After 24 hours, the mice were euthanized, and the major organs were harvested for histological analysis. After being modified with TPP, the probe was primarily excreted by the liver, not the renal. In addition, SOD9-TPP did not show toxicity compared with the control group injected with PBS (fig. S11). Then, in vivo imaging using orthotopic xenograft HNSCC mouse models was further performed (Fig. 5C). The orthotopic HNSCC tumors were verified by small animal 3T magnetic resonance
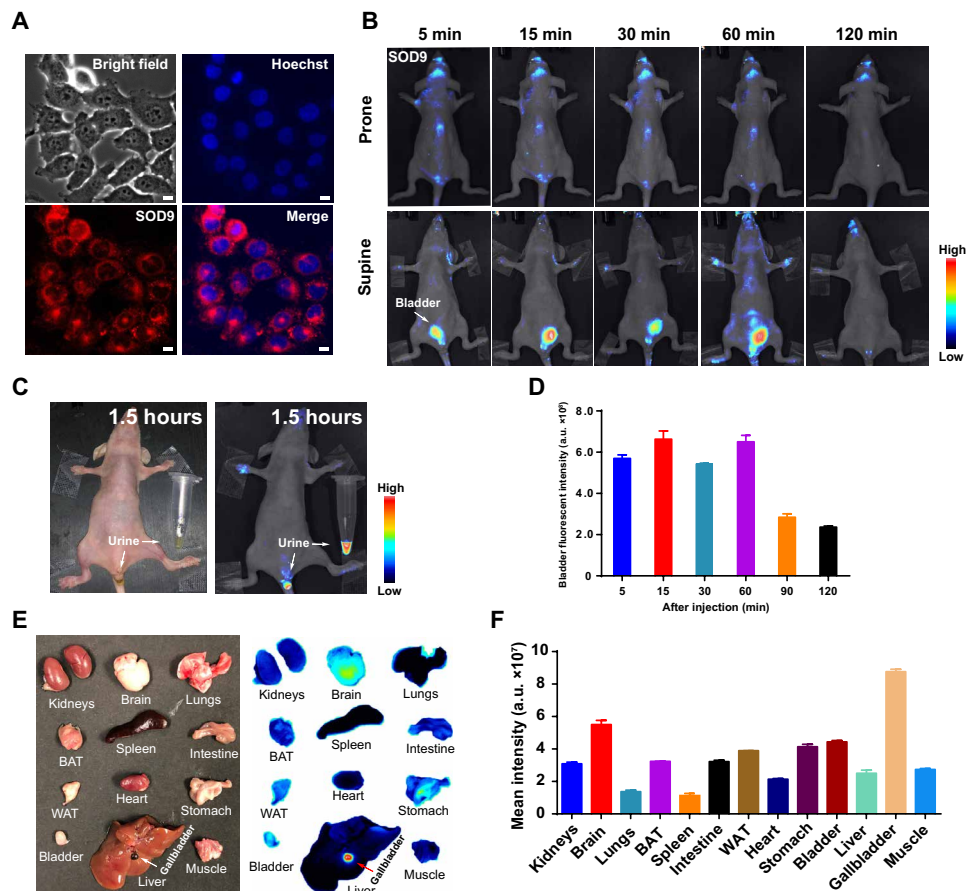
Fig. 4. SOD9's in vivo pharmacokinetics by fluorescence imaging. (**A**) SOD9 fluorescence imaging in NIH-3T3 cell (red) and merge with the nuclear stains Hoechst (blue). Scale bars, 10 μm. (**B**) Whole-body NIR imaging of nude mice ($n = 3$, prone and supine positions) after intravenous injection of SOD9 (2.5 mg/kg, 6.18 μmol/kg). The signal was collected in the 650- to 800-nm channel with an excitation at 500 nm. (**C**) The colored imaging (top) and fluorescence imaging of the nude mice with urine excretion 1.5 hours after intravenous injection of SOD9. (**D**) Comparison of bladder fluorescent intensities at different time points after intravenous injection of SOD9. Error bars, means ± SD ($n = 3$). (**E**) Ex vivo imaging of the major organs dissected after euthanizing animals at 2 hours after intravenous injection of SOD9 (10 mg/kg). Left: colored picture; right: fluorescence imaging. (**F**) Comparison of mean intensities for the major organs at 2 hours after intravenous injection of SOD9. Error bars, means ± SD ($n = 3$).

imaging and pathologic analysis (Fig. 5D). HNSCCs were usually developed from the mucosal epithelium of the oral cavity, pharynx, and larynx, which are the most common malignancies in the head and neck (55). HNSCC of the oral cavity is generally treated with surgical resection, followed by adjuvant radiation and chemotherapy plus radiation, depending on the disease stage. Surgery faces incomplete tumor resection, and radiotherapy suffers severe side effects (56). Fluorescence imaging to guide surgery was considered to play an important role in head and neck cancer therapy due to the improved resection accuracy during surgery (57). At 5 min after intravenous injection of SOD9-TPP (5.0 mg/kg, 6.13 μmol/kg) into the orthotopic HNSCC mice (SCC090 cell line; Fig. 5C), the tumor fluorescent signal was observed with the tumor-to-background ratio (TBR) around 2 (Fig. 5, E and F). The TBR kept stable during the first 30 min postinjection and then reached the maximum, around 3 after 60 min postinjection, followed by a sharp decrease from this moment and kept about 1.5 after 120 min postinjection (Fig. 5, E and F).

Mice were then euthanized, and the major organs were harvested for biodistribution study at 2 hours postinjection. In general, the clearance of SOD9-TPP was much slower than that of SOD9. Although injecting a similar mole dosage (6.1 μmol/kg), almost all

of the SOD9-TPP organ fluorescent intensity was much higher than that of SOD9 (Figs. 4F and 5H). Meanwhile, the fluorescent intensity was the same for the same mole concentration of SOD9 and SOD9-TPP (1.236 mM) solution. Both probes showed up in the mice's brains and gallbladders (Figs. 4E; 5, G and H; and 6F). Since ^{18}F-labeled TPP derivatives were not found in the brain, the BBB passing property was attributed to the SOD9 component (54). SOD9-TPP also accumulated in mice's adrenal glands, intestine, liver, WAT, and BAT (Figs. 5, G and H, and 6F and fig. S12). ^{18}F-labeled TPP derivatives were found in mouse intestines, liver, and adipose tissue. Therefore, this distribution pattern could be partially contributed by TPP moiety in SOD9-TPP. SOD9-TPP was found in the mouse adrenal gland. Notably, SOD9-TPP was not located in the mice's hearts, different from the distribution pattern of the most ^{18}F-labeled TPP positron emission tomography probes (58). SOD9 and TPP's combination changed their in vivo behavior, respectively. The previously unreported probe SOD9-TPP can be used for tumors and the major organ fluorescence imaging.

The above studies found that 60 min postinjection was the best time for fluorescence image–guided tumor surgery. Therefore, we performed the fluorescence image–guided tumor surgery on the orthotopic HNSCC mouse models with in vivo fluorescence imaging
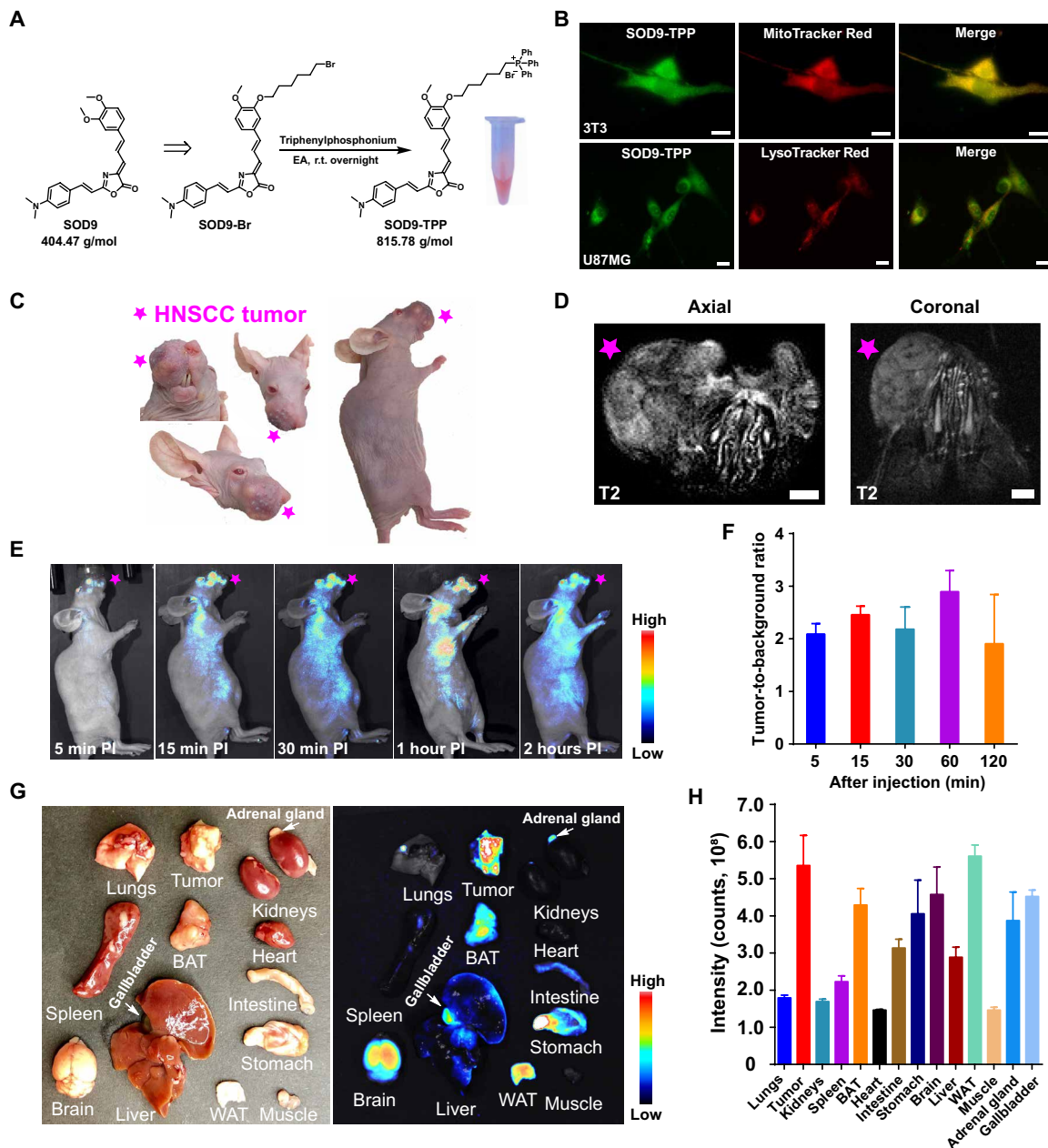
Fig. 5. SOD9-TPP for orthotopic HNSCC tumor imaging. (**A**) The synthesis of SOD9-TPP and the colored pictures of SOD9-TPP dissolved in water. EA, ethyl acetate. (**B**) Colocalization of SOD-TPP, mitochondrial-specific probe (MitoTracker Red), and lysosome-specific probe (LysoTracker Red) in NIH-3T3 and U87MG cell lines. Scale bars, 10 μm. (**C**) The colored picture of the orthotopic HNSCC mouse (SCC090; tumor marked with the red pentagram, the same applies hereinafter). (**D**) 3T magnetic resonance imaging T2 imaging of the mouth of the orthotopic HNSCC mouse. Scale bars, 2 mm. (**E**) Whole-body NIR imaging of the orthotopic HNSCC nude mice ($n = 3$, left lateral position) after intravenous injection of SOD9-TPP (5.0 mg/kg, 6.13 μmol/kg). (**F**) Comparison of the tumor-to-background ratio (TBR) at different time points after intravenous injection of SOD9-TPP. Error bars, means ± SD ($n = 3$). (**G**) Ex vivo imaging of the major organs dissected after euthanizing mice at 48 hours after intravenous injection of SOD9-TPP. Left: Colored picture. Right: Fluorescence imaging. (**H**) Comparison of mean intensities for the HNSCC tumor and the major organs at 48 hours after intravenous injection of SOD9-TPP. Error bars, means ± SD ($n = 3$).

and the on-site pathologic examination using confocal endoscopic microscopy. With suitable dyes, confocal endoscopic microscopy observed pathological organs at cellular morphology in real time, instead of using the traditional procedure with tissue slice and H&E staining. After opening the skin, the tumors were carefully excised under the confocal endoscopic microscopy (Fig. 6A; FIVE2®, ViewnVivo, OptiScan) and the in vivo imaging setup (Fig. 6F; IVIS®,

PerkinElmer). The excised tumors were also imaged by the confocal endoscopic microscopy immediately (Fig. 6A). Current tumor surgery relies on frozen section analysis and gold standard pathologic analysis of formalin-fixed paraffin-embedded sections to identify positive margins intraoperatively (Fig. 6, C to E). It is inconvenient in terms of time and labor consumption during the surgery operation (57). On-site pathologic analysis using confocal endoscopic
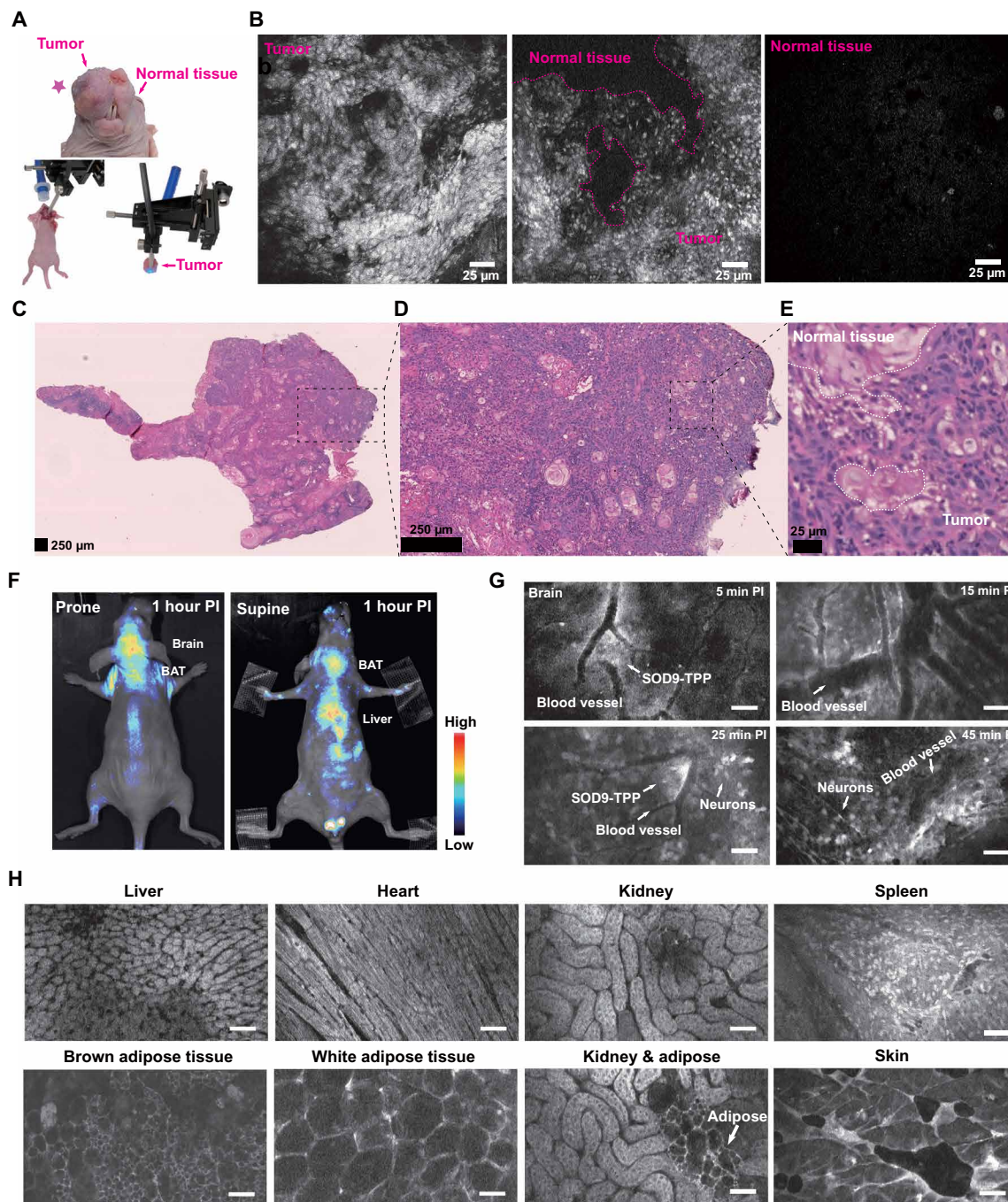
Fig. 6. SOD9-TPP for fluorescence image–guided surgery, brain neuroimaging, and on-site pathologic analysis. (**A**) Top: The colored picture of the orthotopic HNSCC mouse (SCC090; tumor marked with the red pentagram). Bottom left: The setup's color photo of the confocal fluorescent endomicroscopy imaging–guided surgery. Bottom right: The setup's colored photo of the confocal fluorescent endomicroscopy imaging of the resected tissue. (**B**) Confocal fluorescent endomicroscopy imaging of the dissected HNSCC tumor during fluorescence image–guided surgery of the mice 2 hours after intravenous injection of SOD9-TPP (5.0 mg/kg, 6.13 μmol/kg). Right, tumor; middle, tumor and normal tissue; left, normal tissue. (**C**) H&E staining of HNSCC tumor tissue sections. (**D**) The zoomed picture of (C). (**E**) The zoomed picture of (D). (**F**) Whole-body NIR imaging of nude mice ($n = 3$, prone and supine positions) after intravenous injection of SOD9-TPP (5.0 mg/kg, 6.13 μmol/kg); SOD9-TPP was found accumulated in the brain, BAT, and liver. (**G**) Different time points in vivo confocal fluorescent endomicroscopy imaging of brain neurons with the skull opened. Scale bars, 25 μm. (**H**) In vivo confocal fluorescent endomicroscopy imaging of major organs with abdomen and chest opened. Scale bars, 25 μm.

microscopy and tumor-targeted dyes SOD9-TPP may be a good solution. The tumor tissue was found with irregular cell arrangement and high fluorescence intensity, but the normal tissue showed low fluorescence intensity (Fig. 6B and movie S2). The dividing line between them is apparent. Here, pathologic analysis was used to prove the confocal endoscopic microscopy result (Fig. 6, B and C). Meanwhile, the normal tissue was found with a regular cell arrangement shape and relatively low fluorescence intensity (Fig. 6, G and H). It also has the potential to supplement the traditional organ toxicity investigation, which was used to accomplish by histology analysis. SOD9-TPP can be used for fluorescence image–guided tumor surgery and the on-site pathologic analysis to assist the precise resection.

The fast brain accumulation property of SOD9-TPP made it possible for cranial nerve dynamic imaging (Fig. 6, F and G). The mouse brain skull was opened, and the confocal endoscopic microscopy imaging probe was directly put on the brain. Then SOD9-TPP was intravenously injected. The results showed that SOD9-TPP leaked from blood vessels after 5 min postinjection and penetrated deeper tissues in 15 min (movie S3). After that, it approached staining the neuron cell in 25 min. At 45 min later, the original disorderly distributed SOD9-TPPs accumulated into the brain cells. Their strong fluorescence could pinpoint the neurons in the brains (Fig. 6G). This finding highlights that SOD9-TPP can be used for brain nerve dynamic monitoring, which is rarely achieved by most other small molecular dyes. The results should describe the experiments performed and the findings observed. The results section should be divided into subsections to delineate different experimental themes. Subheadings should be descriptive phrases. All data must be shown either here or in the Supplementary Materials.

DISCUSSION

Most reported fluorescent dyes such as rhodamine, BODIPY, FITC, cyanine, coumarin, and quinoline rely on the conjugated system with π electrons and a low energy gap. The absorption and emission wavelength are correlated with the highest occupied molecular orbital (HOMO) and the lowest unoccupied molecular orbital (LUMO). The SOD design was inspired by the redshift seen in the RFP that results from p-HBI chromophore conjugation change and the D-π-A-π-D architecture molecular mechanisms. We have prepared a series of oxazolone analogs and calculated their optimized geometry. The previously unreported structure of dyes shows a lower bandgap, contributing to a larger Stokes shift about 150 to 200 nm than that of traditional fluorescent dyes (<70 nm). Both the substituents and steric hindrance effect play an essential role in the spectroscopic properties of the dyes. SOD9 represents these dyes and proceeds to fluorescence imaging in vivo. It shows good optical and pharmacokinetic properties with high SBR, rapid clearance, and low toxicity. Impressively, SOD9 displays an excellent ability to cross BBB after intravenous injection into mice, providing strong fluorescence to visualize neurons under confocal in vivo fluorescence imaging.

Moreover, SOD9 was modified with a TPP moiety to afford SOD9-TPP, allowing staining of the mitochondria in the living cell. Because of the difference between the mitochondrial activity of normal cells and tumor cells, SOD9-TPP can also be used for tumor imaging, fluorescence navigation surgery, and online tumor tissue identification, with confocal endoscopic microscopy to determine surgical boundaries and reduce surgical trauma. SOD9-TPP has specific strong fluorescence on tumors and the brain in the HNSCC

mouse model. Compared to the traditional pathologic analysis methods, SOD9-TPP and confocal endoscopic microscopy monitor cellular morphology in real time, which simplifies the process of conventional histological examination including the preparation of slices and staining of tissues. They have the possibility to replace some of the complicated H&E staining procedures. SOD9-TPP also provides an opportunity for surgical navigation because of the in vivo tumor targeting ability after intravenous injection. Moreover, these SOD dyes may have many other applications, such as linking with carboxyl groups to label monoclonal antibodies, targeting peptides (Arginylglycylaspartic acid), DNA, and RNA. These further applications are still underway and will be pursued in future research.

In summary, inspired by the p-HBI chromophore change of the GFP/RFP and the D-π-A-π-D architecture molecular mechanisms, we have designed and developed SODs with styrene oxazolone scaffold as previously unreported long Stokes shift fluorescent dyes. Moreover, the most promising dye, SOD9, shows large absorption and emission wavelengths, high quantum efficiency, low cytotoxicity, rapid excretion, and the ability to cross BBB for fluorescence imaging. In addition, TPP-modified SOD9 has a specific and strong targeted fluorescence tumor imaging ability, confirmed by the optical imaging of the HNSCC mouse model and monitoring cellular morphology in real time. SODs are previously unreported and promising scaffold dyes for biomedical fluorescence imaging and surgical navigation.

MATERIALS AND METHODS
Synthesis and characterization of SODs
See the Supplementary Materials for the detailed synthesis characterization information.

SOD derivatives optical properties
Absorbance and fluorescence
Ultraviolet (UV) absorbance of SODs was recorded on an Agilent 8453 UV spectrophotometer at a concentration of 20 μM in water. Fluorescence was recorded on a Fluoromax-3 spectrofluorometer (Jobin Yvon) at a concentration of 12 μM in water.
Optical bandgaps calculated from UV-vis spectra of SODs
On the basis of each SODs' UV–visible (vis) spectrum, the optical bandgap was estimated according to the equation below

$$E_{g(eV)} = h \times f = h \times \frac{c}{\lambda \text{a.e.}} \approx \frac{1240}{\lambda \text{a.e. (nm)}}$$

E_g represents the optical bandgap expressed in electron volts, and λa.e. denotes the absorption edge wavelength expressed in nanometers, obtained from the offset wavelength derived from the low-energy absorption band as schematically represented in fig. S2 (59).
Photostability
A 75-W Xenon arc lamp (Hamamatsu, San Jose, California, USA) with a 420- to 470-nm bandpass filter (MF445-45, Thorlabs, Newton, New Jersey, USA) was used as the light source for the rhodamine 6G. Analogously, a 540- to 580-nm bandpass filter (MF559-34, Thorlabs, Newton, New Jersey, USA) was used to excite SOD derivatives. All the dyes were dissolved in water at a 10 μM concentration in 700 μl of micro quartz cuvettes (10 mm; Sigma-Aldrich, St. Louis, MO, USA). They were continuously excited for 45 min. During this period, the fluorescence intensity was measured every 5 min at 525 (rhodamine 6G) or 600 nm (SOD derivatives). Relative fluorescence intensity change was monitored over time.

Quantum yield

The fluorescence quantum yields of SODs were determined according to the literature in (60)

$$\Phi_x = \Phi_s(F_x/F_s)\,(A_s/A_x)$$

Where Φ is the quantum yield, F is the integrated area under the corrected emission spectrum, and A is the absorbance at the excitation wavelength; the subscripts x and s refer to SODs and the standard, respectively. Rhodamine 6G ($\Phi F = 95\%$) in ethanol was used as the standard. All SODs and rhodamine 6G were dissolved in ethanol in five different concentrations with an absorbance lower than 0.1 at 425 nm. The corresponding five different fluorescences of SODs and rhodamine 6G were excited at 425 nm, and the emission spectra from 450 to 850 nm were obtained for the following integrated area measurement. All data were analyzed using Origin Pro 9.0 software (OriginLab, Northampton, Massachusetts, USA) to get the SODs' final quantum yield.

Cell culture, imaging, and cytotoxicity assay
Cell culture

NIH-3T3 was cultured in a Dulbecco's modified Eagle's medium (DMEM). SCC090 cells were cultured in DMEM containing high glucose (Gibco). U87MG cells were cultured in McCoy's 5A medium. All culture media were supplemented with 10% fetal bovine serum. The cells were incubated at 37°C in an atmosphere containing 5% CO_2. All of the cell lines were obtained from the American Type Tissue Culture Collection (Manassas, VA).

Cell imaging

For the SOD derivatives' live-cell localization imaging, 3 μM SODs in the medium were used to incubate with cells in a MatTek glass-bottom culture dish (Ashland, Massachusetts) for 1 hour, and then the cells were washed with PBS three times. After replacing the medium, the cells were imaged using a fluorescent microscope (Zeiss) with a 20× objective lens (excitation, 453 to 490 nm; emission, 730 to 780 nm).

MitoTracker Red (Molecular Probes) and Hoechst (Thermo Fisher Scientific) were added to the medium to stain the mitochondria and nuclei, following the manufacturer's procedures. Cells were photographed as previously described using a 20× objective lens.

Cytotoxicity assay

The SOD derivatives' toxicity was determined in vitro with an MTT assay (Sigma-Aldrich, St. Louis, MO) on NIH-3T3 cells. Approximately 5000 cells were incubated per well with 200 μl of DMEM growth medium and serially diluted SOD derivative solution ($n = 6$ for each concentration). The cells were kept at 37°C in a humidified atmosphere containing 5% CO_2 for 48 hours in the presence of SOD derivatives at different concentrations. Immediately before adding 20 μl of MTT (5 mg/ml), a colorimetric indicator of cell viability, the SOD derivative–spiked medium was removed from each well plate and replaced with 180 μl of fresh medium. After 4 hours, the medium was carefully removed, and 100 μl of dimethyl sulfoxide (DMSO) was added. Shaking for 10 min, the color change was quantified using a microplate reader (TECAN Infinite M100) and taking absorbance readings at 570 nm with a reference wavelength of 650 nm. Cell viability was plotted as a fraction of the absorbance of control wells incubated without SOD derivatives.

SCC090 orthotopic tumor model and imaging

All vertebrate animals were purchased from Shanghai Experimental Animal Center (Shanghai). All animal procedures were performed under the guideline approved by the Institutional Animal Care and Use Committee of the Shanghai Institute of Materia Medica, Chinese Academy of Sciences. Female athymic nude mice (nu/nu) from 4 to 6 weeks old were obtained from Shanghai Experimental Animal Center (Shanghai) and kept under sterile conditions. The HNSCC cells (SCC090; 5×10^5) were suspended in 15 μl of PBS and inoculated in the nude mice's buccinator.

When the tumors reached ~2 mm in diameter, the tumor-bearing mice were intravenously administered with SOD9-TPP (dissolved in 150 μl of PBS, with 2 μl of DMSO) at 5.0 mg/kg (6.13 μmol/kg). Three mice were used for each group.

In vivo fluorescence imaging was taken at 5, 15, and 30 min and 1 and 2 hours after the injection of SOD9-TPP (5.0 mg/kg, 6.13 μmol/kg). IVIS spectrum instrument was used. The excitation wavelength was set at 535 nm. Collection wavelength was set at 650 to 800 nm, using a 3-s acquisition time. Three mice for each group were used. Mice were euthanized, and the organs were harvested after each set of in vivo imaging. Fluorescence images of the organs and normal mice were taken under the same settings.

Confocal fluorescent endomicroscopy imaging

FIVE2 (ViewnVivo) was used for confocal fluorescent endomicroscopy imaging with the excitation wavelength at 488 nm, and the emission wavelength was taken from 540 nm. In general, the imaging site was opened, and the probe was pressed on the imaged organs' surface.

Histological study

The tumor tissues and major organs such as the liver, kidney, lung, and heart were isolated. After freezing, the specimens were sectioned at 5 to 8 μm and processed for standard H&E staining. Slides were viewed and photographed with the NanoZoomer digital pathology image.

Statistical analysis

GraphPad Prism 5 (GraphPad Software, CA, USA) and SPSS 24.0 software (SPSS Inc., Chicago, IL) were used for statistical analyses. All data are presented as means ± SD of n independent measurements. Statistical analysis was performed using a Student's t test. Statistical significance was assigned for $P < 0.05$.

SUPPLEMENTARY MATERIALS

Supplementary material for this article is available at https://science.org/doi/10.1126/sciadv.abo3289

View/request a protocol for this paper from *Bio-protocol*.

REFERENCES AND NOTES

1. J. Huang, K. Pu, Activatable molecular probes for second near-infrared fluorescence, chemiluminescence, and photoacoustic imaging. *Angew. Chem. Int. Ed. Engl.* **59**, 11717–11731 (2020).
2. G. Hong, A. L. Antaris, H. Dai, Near-infrared fluorophores for biomedical imaging. *Nat. Biomed. Eng.* **1**, 0010 (2017).
3. J. Huang, C. Xie, X. Zhang, Y. Jiang, J. Li, Q. Fan, K. Pu, Renal-clearable molecular semiconductor for second near-infrared fluorescence imaging of kidney dysfunction. *Angew. Chem. Int. Ed. Engl.* **58**, 15120–15127 (2019).
4. J. Zhang, R. E. Campbell, A. Y. Ting, R. Y. Tsien, Creating new fluorescent probes for cell biology. *Nat. Rev. Mol. Cell Biol.* **3**, 906–918 (2002).
5. P. Cheng, K. Pu, Molecular imaging and disease theranostics with renal-clearable optical agents. *Nat. Rev. Mater.* **6**, 1095–1113 (2021).
6. J. Huang, J. Li, Y. Lyu, Q. Miao, K. Pu, Molecular optical imaging probes for early diagnosis of drug-induced acute kidney injury. *Nat. Mater.* **18**, 1133–1143 (2019).
7. N. Y. Baek, C. H. Heo, C. S. Lim, G. Masanta, B. R. Cho, H. M. Kim, A highly sensitive two-photon fluorescent probe for mitochondrial zinc ions in living tissue. *Chem. Commun.* **48**, 4546–4548 (2012).

8. S. K. Bae, C. H. Heo, D. J. Choi, D. Sen, E.-H. Joe, B. R. Cho, H. M. Kim, A ratiometric two-photon fluorescent probe reveals reduction in mitochondrial H2S production in Parkinson's disease gene knockout astrocytes. *J. Am. Chem. Soc.* **135**, 9915–9923 (2013).

9. L. Yuan, W. Lin, Y. Yang, H. Chen, A unique class of near-infrared functional fluorescent dyes with carboxylic-acid-modulated fluorescence on/off switching: Rational design, synthesis, optical properties, theoretical calculations, and applications for fluorescence imaging in living animals. *J. Am. Chem. Soc.* **134**, 1200–1211 (2012).

10. L. Yuan, W. Lin, S. Zhao, W. Gao, B. Chen, L. He, S. Zhu, A unique approach to development of near-infrared fluorescent sensors for in vivo imaging. *J. Am. Chem. Soc.* **134**, 13510–13523 (2012).

11. Y. Koide, Y. Urano, K. Hanaoka, W. Piao, M. Kusakabe, N. Saito, T. Terai, T. Okabe, T. Nagano, Development of NIR fluorescent dyes based on Si-rhodamine for in vivo imaging. *J. Am. Chem. Soc.* **134**, 5029–5031 (2012).

12. A. T. Wrobel, T. C. Johnstone, A. Deliz Liang, S. J. Lippard, P. Rivera-Fuentes, A fast and selective near-infrared fluorescent sensor for multicolor imaging of biological nitroxyl (HNO). *J. Am. Chem. Soc.* **136**, 4697–4705 (2014).

13. N. Karton-Lifshin, E. Segal, L. Omer, M. Portnoy, R. Satchi-Fainaro, D. Shabat, A unique paradigm for a Turn-ON near-infrared cyanine-based probe: Noninvasive intravital optical imaging of hydrogen peroxide. *J. Am. Chem. Soc.* **133**, 10960–10965 (2011).

14. N. Karton-Lifshin, L. Albertazzi, M. Bendikov, P. S. Baran, D. Shabat, "Donor-two-acceptor" dye design: A distinct gateway to NIR fluorescence. *J. Am. Chem. Soc.* **134**, 20412–20420 (2012).

15. T. Myochin, K. Kiyose, K. Hanaoka, H. Kojima, T. Terai, T. Nagano, Rational design of ratiometric near-infrared fluorescent pH probes with various pKa values, based on aminocyanine. *J. Am. Chem. Soc.* **133**, 3401–3409 (2011).

16. Y. Shi, S. Zhang, X. Zhang, A novel near-infrared fluorescent probe for selectively sensing nitroreductase (NTR) in an aqueous medium. *Analyst* **138**, 1952–1955 (2013).

17. J. F. Araneda, W. E. Piers, B. Heyne, M. Parvez, R. McDonald, High stokes shift anilido-pyridine boron difluoride dyes. *Angew. Chem. Int. Ed. Engl.* **50**, 12214–12217 (2011).

18. H. Y. Choi, D. A. Veal, P. Karuso, Epicocconone, a new cell-permeable long Stokes' shift fluorescent stain for live cell imaging and multiplexing. *J. Fluoresc.* **16**, 475–482 (2006).

19. C. Whidbey, N. C. Sadler, R. N. Nair, R. F. Volk, A. J. DeLeon, L. M. Bramer, S. J. Fansler, J. R. Hansen, A. K. Shukla, J. K. Jansson, B. D. Thrall, A. T. Wright, A probe-enabled approach for the selective isolation and characterization of functionally active subpopulations in the gut microbiome. *J. Am. Chem. Soc.* **141**, 42–47 (2019).

20. L. Y. Liu, H. Fang, Q. Chen, M. H. Chan, M. Ng, K. N. Wang, W. Liu, Z. Tian, J. Diao, Z. W. Mao, V. W. Yam, Multiple-color platinum complex with super-large stokes shift for super-resolution imaging of autolysosome escape. *Angew. Chem. Int. Ed. Engl.* **59**, 19229–19236 (2020).

21. T.-B. Ren, W. Xu, W. Zhang, X.-X. Zhang, Z.-Y. Wang, Z. Xiang, L. Yuan, X.-B. Zhang, A general method to increase stokes shift by introducing alternating vibronic structures. *J. Am. Chem. Soc.* **140**, 7716–7722 (2018).

22. A. N. Butkevich, G. Lukinavičius, E. D'Este, S. W. Hell, Cell-permeant large stokes shift dyes for transfection-free multicolor nanoscopy. *J. Am. Chem. Soc.* **139**, 12378–12381 (2017).

23. Y. Qi, Y. Huang, Y. Li, F. Zeng, S. Wu, Real-time monitoring of endogenous cysteine levels in vivo by near-infrared turn-on fluorescent probe with large stokes shift. *Anal. Chem.* **90**, 1014–1020 (2018).

24. C. Sissa, A. Painelli, F. Terenziani, M. Trotta, R. Ragni, About the origin of the large Stokes shift in aminoalkyl substituted heptamethine cyanine dyes. *Phys. Chem. Chem. Phys.* **22**, 129–135 (2019).

25. M. Jiang, X. Gu, J. W. Y. Lam, Y. Zhang, R. T. K. Kwok, K. S. Wong, B. Z. Tang, Two-photon AIE bio-probe with large Stokes shift for specific imaging of lipid droplets. *Chem. Sci.* **8**, 5440–5446 (2017).

26. C. Liu, X. Jiao, Q. Wang, K. Huang, S. He, L. Zhao, X. Zeng, A unique rectilinearly π-extended rhodamine dye with large Stokes shift and near-infrared fluorescence for bioimaging. *Chem. Commun.* **53**, 10727–10730 (2017).

27. M. G. Savelieff, G. Nam, J. Kang, H. J. Lee, M. Lee, M. H. Lim, Development of multifunctional molecules as potential therapeutic candidates for Alzheimer's disease, Parkinson's disease, and amyotrophic lateral sclerosis in the last decade. *Chem. Rev.* **119**, 1221–1322 (2019).

28. L. Belayev, R. Busto, W. Zhao, M. D. Ginsberg, Quantitative evaluation of blood-brain barrier permeability following middle cerebral artery occlusion in rats. *Brain Res.* **739**, 88–96 (1996).

29. G. Sancataldo, L. Silvestri, A. L. A. Mascaro, L. Sacconi, F. S. Pavone, Advanced fluorescence microscopy for in vivo imaging of neuronal activity. *Optica* **6**, 758–765 (2019).

30. F. A. Vuijk, D. E. Hilling, J. S. D. Mieog, A. L. Vahrmeijer, Fluorescent-guided surgery for sentinel lymph node detection in gastric cancer and carcinoembryonic antigen targeted fluorescent-guided surgery in colorectal and pancreatic cancer. *J. Surg. Oncol.* **118**, 315–323 (2018).

31. H. M. Lai, W.-L. Ng, S. M. Gentleman, W. Wu, Chemical probes for visualizing intact animal and human brain tissue. *Cell Chem. Biol.* **24**, 659–672 (2017).

32. M. Gao, F. Yu, C. Lv, J. Choo, L. Chen, Fluorescent chemical probes for accurate tumor diagnosis and targeting therapy. *Chem. Soc. Rev.* **46**, 2237–2271 (2017).

33. M. H. Lee, J. S. Kim, J. L. Sessler, Small molecule-based ratiometric fluorescence probes for cations, anions, and biomolecules. *Chem. Soc. Rev.* **44**, 4185–4191 (2015).

34. S. H. Vargas, C. Lin, H. S. Tran Cao, N. Ikoma, S. AghaAmiri, S. C. Ghosh, A. J. Uselmann, A. Azhdarinia, Receptor-targeted fluorescence-guided surgery with low molecular weight agents. *Front. Oncol.* **11**, 674083 (2021).

35. W. Scheuer, M. van D. Gooitzen, M. Dobosz, M. Schwaiger, V. Ntziachristos, Drug-based optical agents: Infiltrating clinics at lower risk. *Sci. Transl. Med.* **4**, 134ps111 (2012).

36. O. Shimomura, F. H. Johnson, Y. Saiga, Extraction, purification and properties of aequorin, a bioluminescent protein from the luminous hydromedusan, aequorea. *J. Cell. Physiol.* **59**, 223–239 (1962).

37. R. Y. Tsien, The green fluorescent protein. *Annu. Rev. Biochem.* **67**, 509–544 (1998).

38. R. M. Wachter, M. A. Elsliger, K. Kallio, G. T. Hanson, S. J. Remington, Structural basis of spectral shifts in the yellow-emission variants of green fluorescent protein. *Structure* **6**, 1267–1277 (1998).

39. Z. Fan, L. Sun, Y. Huang, Y. Wang, M. Zhang, Bioinspired fluorescent dipeptide nanoparticles for targeted cancer cell imaging and real-time monitoring of drug release. *Nat. Nanotechnol.* **11**, 388–394 (2016).

40. J. Woodhouse, G. N. Kovacs, N. Coquelle, L. M. Uriarte, V. Adam, T. R. M. Barends, M. Byrdin, E. de la Mora, R. B. Doak, M. Feliks, M. Field, F. Fieschi, V. Guillon, S. Jakobs, Y. Joti, P. Macheboeuf, K. Motomura, K. Nass, S. Owada, C. M. Roome, C. Ruckebusch, G. Schirò, R. L. Shoeman, M. Thepaut, M. Togashi, K. Tono, M. Yabashi, M. Cammarata, L. Foucar, D. Bourgeois, M. Sliwa, J.-P. Colletier, I. Schlichting, M. Weik, Photoswitching mechanism of a fluorescent protein revealed by time-resolved crystallography and transient absorption spectroscopy. *Nat. Commun.* **11**, 741 (2020).

41. E. De Zitter, J. Ridard, D. Thédié, V. Adam, B. Lévy, M. Byrdin, G. Gotthard, L. Van Meervelt, P. Dedecker, I. Demachy, D. Bourgeois, Mechanistic investigations of green mEos4b reveal a dynamic long-lived dark state. *J. Am. Chem. Soc.* **142**, 10978–10988 (2020).

42. Z. Gao, Y. Hao, M. Zheng, Y. Chen, A fluorescent dye with large Stokes shift and high stability: Synthesis and application to live cell imaging. *RSC Adv.* **7**, 7604–7609 (2017).

43. X. Wu, X. Sun, Z. Guo, J. Tang, Y. Shen, T. D. James, H. Tian, W. Zhu, In vivo and in situ tracking cancer chemotherapy by highly photostable nir fluorescent theranostic prodrug. *J. Am. Chem. Soc.* **136**, 3579–3588 (2014).

44. M. Staderini, M. A. Martin, M. L. Bolognesi, J. C. Menendez, Imaging of β-amyloid plaques by near infrared fluorescent tracers: A new frontier for chemical neuroscience. *Chem. Soc. Rev.* **44**, 1807–1819 (2015).

45. H. Chen, B. Dong, Y. Tang, W. Lin, A unique "integration" strategy for the rational design of optically tunable near-infrared fluorophores. *Acc. Chem. Res.* **50**, 1410–1422 (2017).

46. M. Sameiro, T. Goncalves, Fluorescent labeling of biomolecules with organic probes. *Chem. Rev.* **109**, 190–212 (2009).

47. P. Crews, J. Rodríguez, M. Jaspars, in *Organic structure analysis*, Topics in organic chemistry (Oxford University Press, 1998), pp. xxiv, 552 p.

48. S. Ashraf, R. Su, J. Akhtar, H. M. Siddiqi, A. Shuja, A. El-Shafei, Effect of fluoro-substituted acceptor-appended ancillary ligands on the photocurrent and photovoltage in dye-sensitized solar cells. *Solar Energy* **199**, 74–81 (2020).

49. H. J. Swatland, Autofluorescence of adipose tissue measured with fibre optics. *Meat Sci.* **19**, 277–284 (1987).

50. S. Bhaumik, J. DePuy, J. Klimash, Strategies to minimize background autofluorescence in live mice during noninvasive fluorescence optical imaging. *Lab Anim.* **36**, 40–43 (2007).

51. G. Masanta, C. S. Lim, H. J. Kim, J. H. Han, H. M. Kim, B. R. Cho, A mitochondrial-targeted two-photon probe for zinc ion. *J. Am. Chem. Soc.* **133**, 5698–5700 (2011).

52. C. Desnous, B. R. Babu, C. Moriou, J. U. O. Mayo, A. Favre, J. Wengel, P. Clivio, The sugar conformation governs (6-4) photoproduct formation at the dinucleotide level. *J. Am. Chem. Soc.* **130**, 30–31 (2008).

53. H. Chen, J. Wang, X. Feng, M. Zhu, S. Hoffmann, A. Hsu, K. Qian, D. Huang, F. Zhao, W. Liu, H. Zhang, Z. Cheng, Mitochondria-targeting fluorescent molecules for high efficiency cancer growth inhibition and imaging. *Chem. Sci.* **10**, 7946–7951 (2019).

54. M. Momcilovic, A. Jones, S. T. Bailey, C. M. Waldmann, R. Li, J. T. Lee, G. Abdelhady, A. Gomez, T. Holloway, E. Schmid, D. Stout, M. C. Fishbein, L. Stiles, D. V. Dabir, S. M. Dubinett, H. Christofk, O. Shirihai, C. M. Koehler, S. Sadeghi, D. B. Shackelford, In vivo imaging of mitochondrial membrane potential in non-small-cell lung cancer. *Nature* **575**, 380–384 (2019).

55. D. E. Johnson, B. Burtness, C. R. Leemans, V. W. Y. Lui, J. E. Bauman, J. R. Grandis, Head and neck squamous cell carcinoma. *Nat. Rev. Dis. Primers.* **6**, 92 (2020).

56. E. de S. Tolentino, B. S. Centurion, L. H. C. Ferreira, A. P. de Souza, J. H. Damante, I. R. F. Rubira-Bullen, Oral adverse effects of head and neck radiotherapy: Literature review and suggestion of a clinical oral care guideline for irradiated patients. *J. Appl. Oral Sci.* **19**, 448–454 (2011).

57. Y. J. Lee, G. Krishnan, N. Nishio, N. S. Berg, G. Lu, B. A. Martin, S. Keulen, A. D. Colevas, S. Kapoor, J. T. C. Liu, E. L. Rosenthal, Intraoperative fluorescence-guided surgery in head and neck squamous cell carcinoma. *Laryngoscope* **131**, 529–534 (2021).

58. J. Zielonka, J. Joseph, A. Sikora, M. Hardy, O. Ouari, J. Vasquez-Vivar, G. Cheng, M. Lopez, B. Kalyanaraman, Mitochondria-targeted triphenylphosphonium-based compounds: Syntheses, mechanisms of action, and therapeutic and diagnostic applications. *Chem. Rev.* **117**, 10043–10120 (2017).

59. J. C. S. Costa, R. J. S. Taveira, C. F. R. A. C. Lima, A. Mendes, L. M. N. B. F. Santos, Optical band gaps of organic semiconductor materials. *Opt. Mater.* **58**, 51–60 (2016).

60. R. A. Velapoldi, H. H. Tønnesen, Corrected emission spectra and quantum yields for a series of fluorescent compounds in the visible spectral region. *J. Fluoresc.* **14**, 465–472 (2004).